ROYAL SOCIETY
OF CHEMISTRY

PAPER

CrossMark
← click for updates

Structure–property relationships for bis-diketopyrrolopyrrole molecules in organic photovoltaics†

Qiang (Mike) Wang,[ab] Jacobus J. van Franeker,[ab] Bardo J. Bruijnaers,[a] Martijn M. Wienk[ac] and René A. J. Janssen*[ac]

The design of small organic molecules for efficient solution-processed organic solar cells is hampered by the absence of relationships that connect molecular structure *via* processing to blend morphology and power conversion efficiency. Here we study a series of bis-diketopyrrolopyrrole molecules in which we systematically vary the aromatic core, the solubilizing side chains, and the end groups to achieve power conversion efficiencies of 4.4%. By comparing the morphology and performance we attempt to identify and rationalize the structure–property relationships. We find that the tendency to aggregate or crystallize are important factors to control and that these require a subtle balance.

1. Introduction

The surge in power conversion efficiency (PCE) of organic photovoltaic (OPV) cells in the last decade has primarily been achieved by developing new organic semiconductors that feature high charge carrier mobilities and carefully tuned frontier molecular orbital (HOMO and LUMO) levels to maximize the open-circuit voltage and short-circuit current. The progress further relied on optimizing the phase separation between the donor and acceptor materials *via* judicious processing to achieve high current densities and fill factors. The highest reported efficiencies for single junction polymer solar cells exceed 10%.[1–6] One drawback of synthetic semiconducting polymers is their statistically determined nature, reflected – amongst others – in their molecular weight distribution and the occurrence of undesired homo-coupling reactions during the polymerization.[7–10]

Small conjugated molecules and well-defined oligomers of intermediate dimensions with distinct molecular structures and controllable purity alleviate the lack of chemical and structural definition of conjugated polymers.[11,12] Using well-defined oligomers and reproducible processing methods, improved understanding of structure–property relationships can be anticipated.[13] Solution-processed small-molecule organic solar cells were first described for oligothiophenes,[14]

merocyanines,[15] and squaraine dyes.[16] Presently the highest PCEs of solution-processed small-molecule organic solar cells rival those of the most efficient polymer solar cells.[17–19] A common design element of these efficient molecules is that they are based on complementary electron rich (donor, D) (mostly thiophene based) and electron deficient (acceptor, A) units in D–A–D or A–D–A motifs.

To extend the spectral coverage to the near infrared, organic semiconductors based on diketopyrrolopyrrole (DPP) have been applied in organic solar cells.[20–23] DPP polymers exhibit high charge carrier mobilities, which add to their suitability for application in solar cells.[24,25] Also small molecules incorporating a DPP unit have extensively been investigated for use in organic solar cells.[26–42] Among the many DPP molecules that have been considered for use in organic solar cells, those incorporating the A–D–A or D–A–D–A–D motifs with DPP as acceptor unit have been very popular.[43–104] By introducing extended planar aromatic donor bridges between the two DPP acceptor units it is possible to obtain high charge mobility and to manipulate the energies of the frontier orbitals to control voltage and charge transfer to the fullerene acceptor. Several bis-DPP molecules afford PCEs up to 6%, and some even higher.[72,87,90] The record PCE of 8.08% for a solution-processed small-molecule solar cell based on DPP units has been obtained for a compound comprising two DPP units linked to a central porphyrin *via* acetylene bonds.[90]

In all bulk-heterojunction organic solar cells the morphology of the blend and the nanoscale phase separation is crucial to achieve efficient exciton dissociation into charge carriers and to provide suitable percolating pathways to transport charges to the electrodes. Undoubtedly, achieving an optimized morphology is the key to unlock the full potential of the small-molecule organic donors. While this is well recognized in the field, there is

aMolecular Materials and Nanosystems, Institute for Complex Molecular Systems, Eindhoven University of Technology, P. O. Box 513, 5600 MB Eindhoven, The Netherlands. E-mail: r.a.j.janssen@tue.nl

bDutch Polymer Institute (DPI), P. O. Box 902, 5600 AX Eindhoven, The Netherlands

cDutch Institute for Fundamental Energy Research, De Zaale 20, 5612 AJ Eindhoven, The Netherlands

† Electronic supplementary information (ESI) available: Additional graphs and tables. See DOI: 10.1039/c6ta01533f

This journal is © The Royal Society of Chemistry 2016

Fig. 1 Structures of bis-DPP molecules.
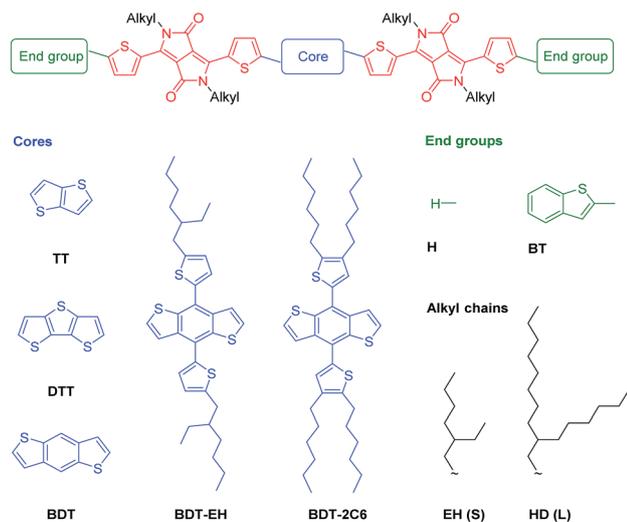
| Name	Core	End group	Alkyl chain
TT-S	TT	H	EH
DTT-S	DTT	H	EH
DTT-L	DTT	H	HD
BDT-S	BDT	H	EH
BDT-L	BDT	H	HD
BDT-EH-S	BDT-EH	H	EH
BDT-2C6-S	BDT-2C6	H	EH
BDT-EH-S-BT	BDT-EH	BT	EH

little general knowledge on how the molecular structure directs the blend morphology and how this is influenced by processing conditions such as solvent, co-solvent, and thermal annealing. In this paper we present a series of bis-DPP molecules with A–D–A and D–A–D–A–D motifs with different central cores, solubilizing side chains, and end groups connected to the two DPP units (Fig. 1). The series of molecules was designed to provide similar optical band gaps and HOMO and LUMO levels, to focus on effects of the structural changes in the different parts of the bis-DPP molecules on performance and morphology. The results contribute to establishing structure–performance relationships for solution-processed small-molecule organic solar cells.

2. Results and discussion

2.1. Synthesis

The bis-DPP molecules shown in Fig. 1 were synthesized *via* Stille reactions using the appropriate bis(trimethyltin)-substituted aromatic core and 3-(5-bromothiophen-2-yl)-2,5-bis(dialkyl)-6-(thiophen-2-yl)-2,5-dihydropyrrolo[3,4-*c*]pyrrole-1,4-dione in toluene at 115 °C using tris(dibenzylideneacetone) dipalladium(0) as a catalyst (Scheme 1). For BDT-EH-S-BT, 3-(5-(benzo[*b*]thiophen-2-yl)thiophen-2-yl)-6-(5-bromo-thiophen-2-yl)-2,5-bis(2-ethylhexyl)pyrrolo[3,4-*c*]pyrrole-1,4-dione was used instead. All products were purified *via* column chromatography or preparative recycling gel permeation chromatography and characterized with NMR and MALDI-TOF mass spectrometry.
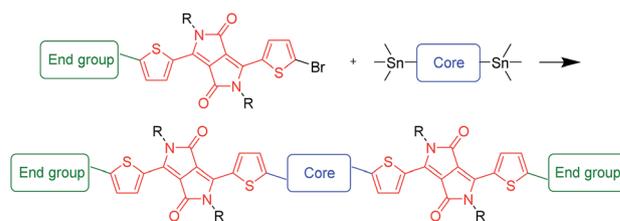
Scheme 1 Generalized synthetic procedure of the bis-DPP molecules.

The details of the synthesis and characterization of the molecules shown in Fig. 1 can be found in the ESI†.

2.2. Optical absorption

The UV-vis absorption spectra of the bis-DPP molecules in solution are similar (Fig. 2a). The optical absorption of bis-DPP molecules with a benzo[1,2-*b*:4,5-*b'*]dithiophene (BDT) core is slightly hypsochromically shifted with respect to those of the thieno[3,2-*b*]thiophene (TT) and dithieno[3,2-*b*:2′,3′-*d*]thiophene (DTT) cores. The five bis-DPP derivatives with a BDT core show a vibronic transition at lower wavelengths, whereas the other bis-DPPs show a featureless absorption band. The two benzo[*b*]thiophen-2-yl (BT) end groups in BDT-EH-S-BT cause a substantial bathochromic shift, compared to BDT-EH-S. On the other hand, the two 2-thienyl substituents on the 4 and 8 positions of BDT have a negligible effects on the optical absorption in solution.
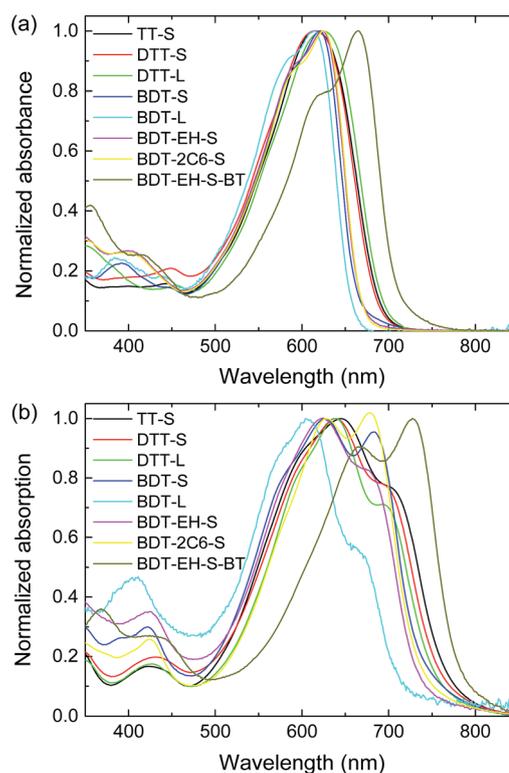

Fig. 2 UV-vis absorption spectra of bis-DPP molecules shown in Fig. 1 in (a) solution and (b) thin films.

In thin solid films all compounds exhibit a substantial bathochromic shift of the optical absorption and all compounds show fine structure as a consequence of vibronic transitions and coupling of transition dipoles (Fig. 2b) of nearby molecules. The magnitude of the bathochromic shift in thin films is similar for all bis-DPPs, except for BDT-L which is less shifted. The relative intensity of the longest wavelength absorption band is the highest for BDT-EH-S-BT and then reduces along the series BDT-2C6-S, BDT-S, BDT-EH-S, TT-S and DTT-S to lower values for DTT-L and BDT-L. A low relative intensity of the longest wavelength absorption band in the solid state can point to the formation of H-type aggregates.[39] Especially for BDT-L, for which λ_{max} in solution (614 nm) is larger than in the film (604 nm), the optical absorption is reminiscent of an H-type aggregate in the film.

Cyclic voltammetry was performed in dichloromethane to determine the frontier orbital energy levels of the bis-DPP molecules (Fig. 3). The corresponding cyclic voltammograms are collected in Fig. S1 (ESI†) and show that the oxidation and reduction waves are in general chemically reversible. The electrochemical band gaps determined from the differences between the potentials at the onsets of the redox waves are similar to the optical band gaps determined from the onsets of absorption (in the solution spectra) (Table 1), but consistently somewhat smaller. From the cyclic voltammetry we find that the HOMO levels of the bis-DPP molecules are at −5.515 (±0.03) eV, using −5.23 eV vs. vacuum for the ferrocene/ferrocenium redox couple. Based on these small differences in the oxidation potentials, no large differences are expected in the open-circuit voltage (V_{oc}) of the solar cells based on these bis-DPP molecules.

2.3. Solar cells and morphologies

Organic solar cells were fabricated by sandwiching a bulk heterojunction of the bis-DPP molecules and [60]PCBM between a transparent ITO/PEDOT:PSS front electrode and a LiF/Al back electrode on glass substrates. The active layer was deposited via spin coating from chloroform with and without co-solvents. All photoactive layers were extensively optimized for their photovoltaic performance by adjusting the solvent mixture, spin speed, and applying thermal annealing conditions. An overview of the most relevant data can be found in Tables S1–S8 (ESI†). The ESI† also contains the current density–voltage (J–V) characteristics and the external quantum efficiencies (EQEs) of the optimized devices.

2.3.1 Effect of central core. Among the bis-DPP molecules shown in Fig. 1, there are three different electron-rich aromatic cores TT, DTT, and BDT. Solar cells of these molecules blended with [60]PCBM were optimized for co-solvent and thermal annealing. Adding 0.2% 1-chloronapthalene (1-CN) as co-solvent in chloroform, gave better performance than using o-dichlorobenzene (o-DCB) or 1,8-diiodooctane (DIO) for all three blends. Thermal annealing (110 °C, 10 min.) improved the TT-S:[60]PCBM cells by about 25%, but resulted in a 50% or more loss in performance for the DTT-S:[60]PCBM and BDT-S:[60]PCBM cells.

In Table 2 we compare the photovoltaic parameters of the optimized devices of TT-S, DTT-S and BDT-S mixed with [60]PCBM in a 1 : 1 weight ratio. The highest PCE = 4.3% is found

Table 2 Best-performance devices of TT-S, DTT-S, and BDT-S mixed with [60]PCBM in a 1 : 1 ratio[a]

Material	Annealing	J_{sc} (mA cm^{-2})	V_{oc} (V)	FF	PCE (%)
TT-S	110 °C 10 min	9.46	0.81	0.56	4.3
DTT-S	No	6.82	0.76	0.44	2.3
BDT-S	No	5.95	0.85	0.53	2.7

[a] Spin coated from chloroform containing 0.2% 1-CN.

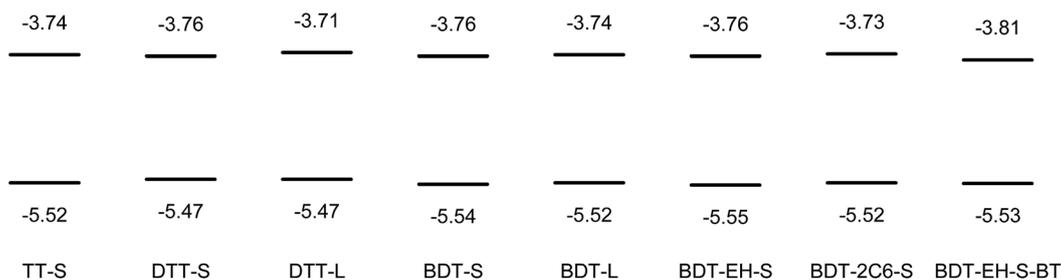|	TT-S	DTT-S	DTT-L	BDT-S	BDT-L	BDT-EH-S	BDT-2C6-S	BDT-EH-S-BT
	−3.74	−3.76	−3.71	−3.76	−3.74	−3.76	−3.73	−3.81
	−5.52	−5.47	−5.47	−5.54	−5.52	−5.55	−5.52	−5.53

Fig. 3 Energy levels (in eV vs. vacuum) of bis-DPP molecules measured by cyclic voltammetry.

Table 1 Electrochemical and optical band gaps and absorption maxima and onsets of the bis-DPP molecules in solution

Molecule	TT-S	DTT-S	DTT-L	BDT-S	BDT-L	BDT-EH-S	BDT-2C6-S	BDT-EH-S-BT
E_g^{CV} (eV)	1.78	1.71	1.76	1.78	1.78	1.79	1.79	1.72
λ_{max} (nm)	616	615	623	620	614	624	625	666
λ_{onset} (nm)	689	684	691	662	657	669	669	711
E_g (eV)	1.80	1.81	1.79	1.87	1.89	1.85	1.85	1.74

10534 | J. Mater. Chem. A, 2016, **4**, 10532–10541

This journal is © The Royal Society of Chemistry 2016

for TT-S:[60]PCBM, similar to the value of 4.0% reported previously for this compound.[61] This layer possesses the highest short-circuit current density (J_{sc}) and fill factor (FF) of the three derivatives. The EQE of the TT-S:[60]PCBM cells reaches a maximum of 49% (Fig. S2a, ESI†).

Atomic force microscopy (AFM) height and phase images of the TT-S:[60]PCBM blend (Fig. S11, ESI†) reveal the presence of fibrous surface features and a root-mean-square surface roughness (R_q) of 6.9 nm. In transmission electron microscopy (TEM), however, the TT-S:[60]PCBM blend shows little contrast (Fig. 4a and S2b in the ESI†), suggesting intimate mixing, without large scale phase separation.

The DTT-S:[60]PCBM solar cell (PCE = 2.3%) has a lower FF, J_{sc} and EQE (37%) than the optimized TT-S:[60]PCBM device. The photocurrent is strongly bias dependent and reaches a similar value as the photocurrent in the TT-S:[60]PCBM cell at a reverse bias of −1.5 V (cf. Fig. S2a and S3a in the ESI†). This demonstrates that exciton dissociation into charge-transfer states is similar in the two blends, but that charge extraction is more difficult in the DTT-S:[60]PCBM blend. This can be due to the much lower hole mobility of DTT-S (10^{-4} cm^2 V^{-1} s^{-1}) compared to TT-S (0.1 cm^2 V^{-1} s^{-1}), which has been reported in

field-effect transistors of these materials.[105] A low hole mobility reduces the rate at which photogenerated charge-transfer states dissociate into free charges and can also reduce the fill factor if the charge transport of electrons and holes is unbalanced.[106] A second possible reason for the low FF and the observed field-assisted photocurrent collection is the absence of a percolating phase of DTT-S molecules, such that charge transport is hampered. Consistently, the TEM images of as-cast DTT-S:[60]PCBM blends (Fig. 4b, and S3b in the ESI†) do not show significant phase separation.

For BDT-S:[60]PCBM blends (PCE = 2.8%), the FF is enhanced compared to DTT-S:[60]PCBM, but the photocurrent and maximum EQE (31%) are lower and do not significantly increase in reverse bias (Fig. S4a, ESI†). Hence, charges are generated less efficiently than in the other two blends but are relatively easily transported. This would be consistent with a more phase-separated morphology in which pure domains facilitate charge transport but where a decreased donor–acceptor interface area reduces the exciton dissociation. The TEM images of the BDT-S:[60]PCBM blend (Fig. 4c, and S4b in the ESI†), however, do not show distinct evidence of such coarser phase separation, although there is contrast on larger length scales than in the blends of TT-S and DTT-S with [60]PCBM.

2.3.2 Effect of side chain on DPP. To investigate the effect of side chain length and solubility, we synthesized DTT-L and BDT-L with longer 2-hexyldecyl side chains. Optimized devices of DTT-L with [60]PCBM show a higher PCE than the corresponding short-side chain DTT-S (cf. Tables 2 and 3). The increase is due to a slightly higher V_{oc} and considerably improved fill factor. The higher V_{oc} of the solar cells based on DTT when longer side chains are used on the DPP units is possibly related to the smaller bathochromic shift going from solution to film and the concomitant wider optical band gap. The wider optical band gap of DTT-L will deepen the HOMO energy level and increase open-circuit voltage. For BDT-L:[60]PCBM the overall performance is very similar to that of BDT-S:[60]PCBM. Both provide a PCE of 2.7%, but with rather low maximum EQEs of 32% and 34%, respectively (Fig. S5a and S6a, ESI†).

The fill factor of 0.60 of the DTT-L:[60]PCBM cell is comparatively high for a solution-processed small molecule solar cell and much higher than the value of 0.44 for the short chain DTT-S:[60]PCBM blends. Compared to the intimately mixed DTT-S:[60]PCBM blend, the DTT-L:[60]PCBM films display distinct contrast on a length scale of less than 50 nm in TEM (Fig. 4d and S5b in the ESI†). This coarser phase
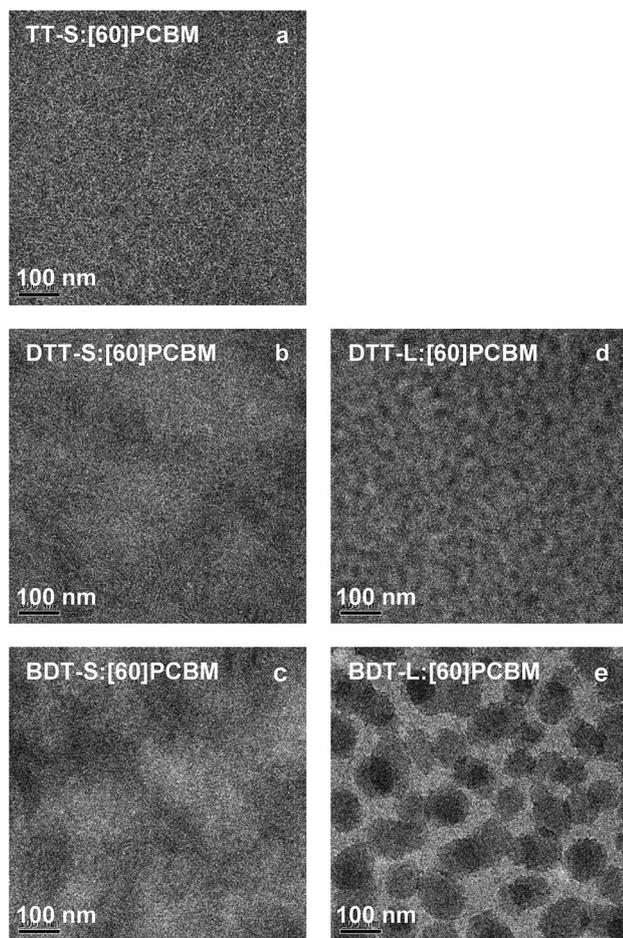

Fig. 4   TEM images of optimized photoactive layers of (a) TT-S:[60]PCBM, (b) DTT-S:[60]PCBM, (c) BDT-S:[60]PCBM, (d) DTT-L:[60]PCBM, and (e) BDT-L:[60]PCBM.

Table 3   Best-performance devices of DTT-L and BDT-L mixed with [60]PCBM in a 1 : 1 ratio[a]

Material	Annealing	J_{sc} (mA cm^{-2})	V_{oc} (V)	FF	PCE (%)
DTT-L	No	5.83	0.81	0.60	2.8
BDT-L	No	5.53	0.85	0.58	2.7

[a] Spin coated from chloroform containing 0.2% 1-CN.

separation improves percolation of charges and enhances the fill factor.

Also the morphology of BDT-L:[60]PCBM films shows large (~100 nm) darker [60]PCBM rich domains (Fig. 4e and S6b in the ESI†) in TEM. These images are reminiscent of the polymer–fullerene morphologies in which spinodal liquid–liquid demixing occurs before the film is dry.[107] For polymer–fullerene bulk heterojunctions this predominantly happens under conditions where the polymer has good solubility and aggregation only occurs in the last stages of film drying.[108] This is consistent with the present result where long side chains impart increased solubility on BDT-L compared to BDT-S. In the regions in between the dark [60]PCBM domains the blend has distinct crystalline domains as inferred from the lattice fringes in the TEM images (Fig. S6b, ESI†). The main lattice spacing estimated from the Fourier transform of the TEM image is 1.9 ± 0.1 nm (Fig. S6b, ESI†) and corresponds to the value of 2.0 nm of pure BST-L inferred from the X-ray diffraction at $2\theta = 4.40°$ (Fig. S14, ESI†).

We see that for these two examples the longer side chains result in a coarser and more distinct phase separation with [60]PCBM as compared to the blends of the same compounds with shorter side chains. In analogy with previously studied polymer–fullerene blends we attribute this effect to an increased solubility. There are two effects that play as role. First, a higher solubility implies that spinodal liquid–liquid demixing can occur before the molecules aggregate or crystallize.[108] This results in large, almost pure domains as seen in the BDT-L:[60]PCBM films. Second, the critical size at which a nucleus becomes stable against re-dissolving is larger for more soluble molecules. Hence, phase separation with narrow fibres and small crystallites can be expected for less soluble compounds.[109]

2.3.3 Effect of side chain on central core. An alternative method to modify the solubility of the bis-DPPs is by introducing side chains on the aromatic core. For this reason we studied BDT-EH-S and BDT-2C6-S which possess the same π-conjugated backbone and side chains on the DPP units as BDT-S, but have alkyl-substituted 2-thienyl groups on the central BDT core (Fig. 1). TEM reveals that spin coating blends of both molecules with [60]PCBM from chloroform containing 0.2% 1-CN results in an intimately mixed morphology (Fig. 5a and c) which results in PCEs of 2.4% and 1.1% (Table 4) for the corresponding solar cells.

After thermal annealing, the BDT-EH-S:[60]PCBM film shows small but distinguishable domain features in TEM (Fig. 5b and S8b ESI† for TEM at higher magnification) and a significantly increased PCE of 4.4%, mainly as a result of an increased photocurrent and fill factor. The maximum EQE is 52% (Fig. S8a, ESI†). For BDT-EH-S:[60]PCBM films a higher PCE of 5.79% has been reported for a layer processed from chloroform and annealed at 110 °C for 10 min.[53] The photovoltaic parameters of the reported record device ($J_{sc} = 11.97$ mA cm^{-2}, $V_{oc} = 0.84$ V, FF = 0.576)[53] show that the main difference with our result is a higher short-circuit current. In our hands processing from chloroform in combination with thermal annealing gave PCE = 4.3% (Table S6, ESI†).
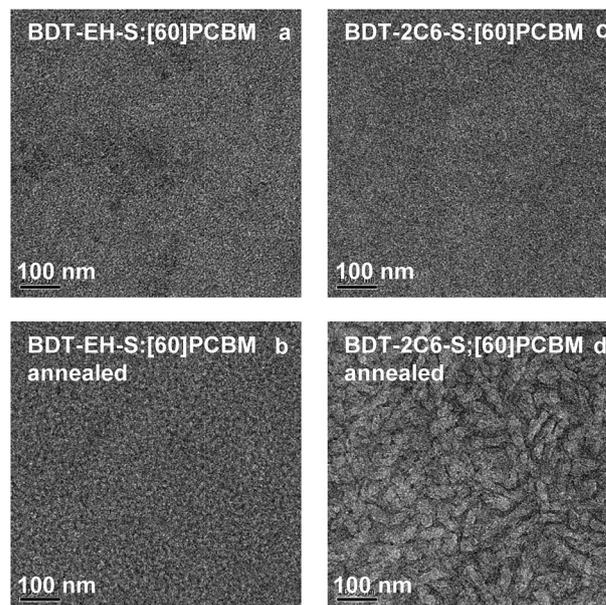

Fig. 5 TEM images of optimized photoactive layers of BDT-EH-S (a and b) and BDT-2C6-S (c and d) spin coated from chloroform containing 0.2% 1-CN before (a and c) and after (b and d) thermal annealing at 110 °C for 10 min.

Table 4 Best-performance devices of BDT-EH-S. BDT-2C6-S and BDT-EH-S-BT mixed with [60]PCBM in a 1 : 1 ratio

Materials	Annealing	J_{sc} (mA cm^{-2})	V_{oc} (V)	FF	PCE (%)
BDT-EH-S[a]	No	6.76	0.92	0.39	2.4
BDT-EH-S[a]	110 °C 10 min	9.36	0.83	0.56	4.4
BDT-2C6-S[a]	No	3.59	0.97	0.30	1.1
BDT-2C6-S[a]	110 °C 10 min	2.43	0.86	0.29	0.6
BDT-2C6-S[b]	No	5.67	0.80	0.56	2.5
BDT-EH-S-BT[c]	110 °C 10 min	9.90	0.77	0.56	4.3

[a] Spin coated from chloroform containing 0.2% 1-CN. [b] Spin coated from chloroform containing 0.3% 1,8-diiodooctane. [c] Spin coated from pure chloroform.

Thermal annealing of the BDT-2C6-S:[60]PCBM films, on the other hand, results in a significant loss of the PCE, mainly due to a loss of photocurrent and a fill factor that remains low. In TEM the BDT-2C6-S:[60]PCBM active layer exhibits large worm-like domains after thermal annealing (Fig. 5d and S9b ESI† for TEM at higher magnification). The increased domain size can explain the lower photocurrent, but does not explain the very low FF, which might be due to the absence of percolating pathways for charges.

The TEM images in Fig. 5 show that in the blends of BDT-EH-S and BDT-2C6-S with [60]PCBM the degree of phase separation is similar directly after spin coating from chloroform containing 0.2% 1-CN, but that thermal annealing results in much larger domains for BDT-2C6-S:[60]PCBM than for BDT-EH-S:[60]PCBM. The difference is likely related to the different tendency of the two molecules to crystallize. X-ray diffraction (XRD) on

10536 | *J. Mater. Chem. A*, 2016, **4**, 10532–10541

This journal is © The Royal Society of Chemistry 2016

pure (*i.e.* without [60]PCBM) drop-cast films of BDT-EH-S and of BDT-2C6-S shown in Fig. 6 reveals that the main diffraction peak is much more intense for BDT-2C6-S than for BDT-EH-S. This lends support to the conclusion from TEM that BDT-2C6-S crystallizes more easily than BDT-EH-S. The TEM results indicate that in as-cast films the crystallization of bis-DPP molecules is reduced in the presence of [60]PCBM and that the extent to which crystallization can be enhanced by thermal annealing depends on the molecular structure.

Table 4 shows that both the BDT-EH-S:[60]PCBM and BDT-2C6-S:[60]PCBM solar cells have a ~100 mV lower open-circuit voltage after thermal annealing of the active layer. We attribute this to the aggregation of the two molecules and a concomitant shift of frontier orbital energy levels. In the XRD of the pure BDT-2C6-S films we see a narrowing and shift of the diffraction peak of BDT-2C6-S after annealing. The shift indicates a change of the lattice constants and crystal structure.

The best performance for BDT-2C6-S:[60]PCBM (PCE = 2.5% and maximum EQE = 36%) was obtained when the layer was spin coated from chloroform containing 0.3% 1,8-diiodooctane (DIO) (Table 4). The increase in J_{sc} and FF and concomitant decrease in V_{oc} for this device as compared to the un-annealed layer from chloroform containing 0.2% 1-CN, suggest that the use of DIO enhances the formation of crystalline domains.

2.3.4 End group extension. So far BDT-EH-S has provided the highest PCE in this study. The molecule can be further extended with benzo[*b*]thiophen-2-yl (BT) units on both sides (Fig. 1). The optimized device of BDT-EH-S-BT with [60]PCBM shows a slightly higher short-circuit current density but a correspondingly smaller open-circuit voltage than that of BDT-EH-S (Fig. 7a), while the fill factors and the overall efficiencies are almost the same (Table 4). Also the maximum EQEs (52% *vs.*
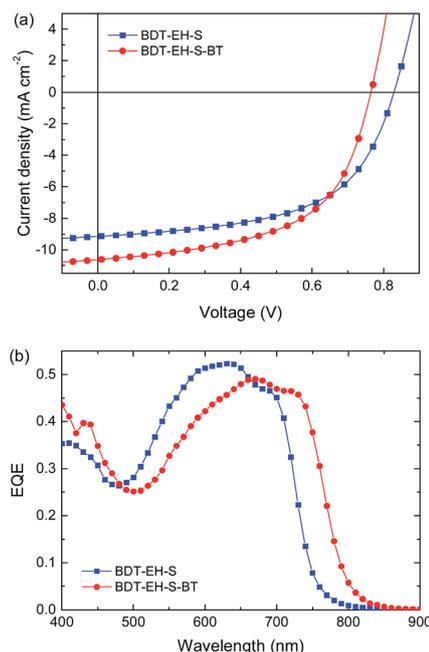

Fig. 7 (a) *J*–*V* characteristics and (b) EQE of optimized devices of BDT-EH-S and BDT-EH-S-BT with [60]PCBM.

49%, Fig. 7b) are very close. TEM images show virtually identical morphologies for the two blends (Fig. 8). The small difference in short-circuit current density can be related to the different optical band gaps, which are 1.65 and 1.55 eV for BDT-EH-S and BDT-EH-S-BT, respectively as determined from the onset of the EQEs in the thin films (Fig. 7b). The smaller optical band gap provides a better overlap with the photon flux of the AM1.5G solar spectrum, resulting in an increased J_{sc}. The reduction of the V_{oc} for BDT-EH-S-BT indicates that in the solid state the energy difference between the highest occupied molecular orbital (HOMO) level of the bis-DPP and the lowest unoccupied molecular orbital (LUMO) level of the [60]PCBM acceptor is smaller than for BDT-EH-S. In solution, however, the oxidation potentials of the two compounds are virtually identical (Fig. 3).

2.3.5 Effect of the co-solvent. Most bis-DPP molecules in this study exhibited the highest PCE in photoactive layers with [60]PCBM when deposited from chloroform with 0.2% 1-CN as
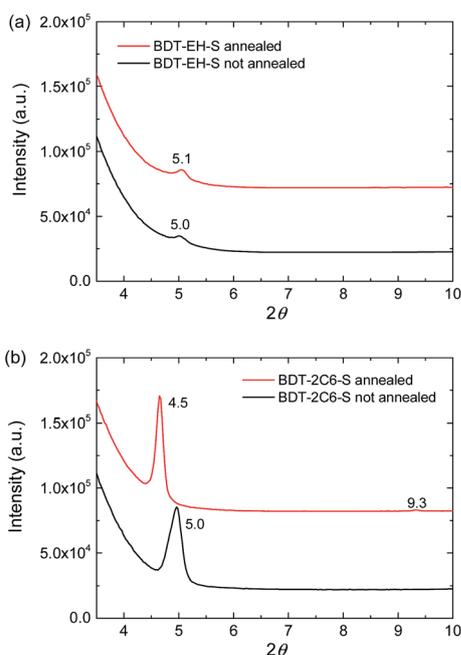

Fig. 6 X-ray diffractograms of thin films of (a) BDT-EH-S and (b) BDT-2C6-S before and after thermal annealing.
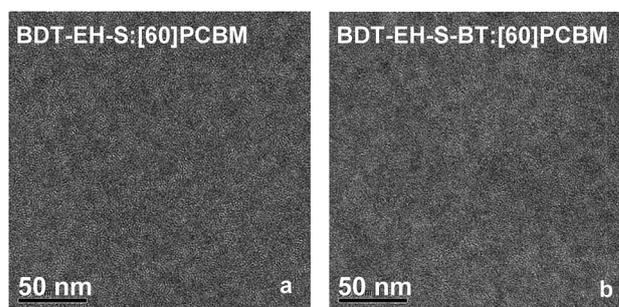

Fig. 8 TEM images of optimized photoactive layers of BDT-EH-S (a) and BDT-EH-S-BT (b) with [60]PCBM after thermal annealing at 110 °C for 10 min.

co-solvent. In Table 5 we compare the effect of 1-CN, DIO, and o-DCB as co-solvents in mixtures with chloroform for blends of the bis-DPP molecules with [60]PCBM. The results do not show a clear trend, although in most cases the use of 1-CN has a beneficial effect on the PCE. The efficiency of the bis-DPP:[60]PCBM devices presented in Table 5, is primarily determined by the combination of the molecular structure and nature of the co-solvent, and considerable fine tuning of this combination is required for device optimization.

The role of the co-solvent in solution-processed small-molecule solar cells remains a point of discussion. A very strong dependence of the PCE on subtle changes in the amount of co-solvent has been noted before for small-molecule bulk-heterojunctions solar cells,[110] but also less pronounced effects have been reported.[111] For DPP-based polymers it was recently shown that the solubility of the DPP-polymer determines the width of the polymer fibrils formed.[109] Co-solvents that provide a lower solubility for the DPP-polymer, gave smaller domain sizes and higher PCEs. In general the effect of the co-solvent for the bis-DPP:[60]PCBM mixtures is less outspoken than for the polymers and there is no obvious trend in the data. There is an important difference, between co-solvents used for small-molecule and for polymer solar cells. The amount of co-solvent that gives optimized performance is smaller for bis-DPP small molecules (~0.2 vol%) than for DPP polymer solar cells (>3 vol%). Because the co-solvents have a lower evaporation rate than the main solvent, this implies that for polymer solar cells the last phase of film drying where the main solvent has evaporated, the deposition is almost exclusively from the co-solvent. In contrast, for small-molecule bis-DPPs, where the amount of co-solvent is a factor of ten less, the primary solvent plays a significant role during the entire deposition. In fact, for the bis-DPP molecules the optimal amount of co-solvent of about 0.2 vol% (corresponding to 2.4 to 3.6 mg ml^{-1}, depending on the co-solvent) is less than the concentration of the semiconductors (typical total concentration used 10–20 mg ml^{-1}).

2.3.6 Effect of thermal annealing. For the optimized solvent/co-solvent deposition conditions, the device performance with or without thermal annealing is compared in Table 6. Thermal annealing is beneficial for TT-S, BDT-EH-S and BDT-EH-S-BT. In each of these cases the as-cast film exhibits little or no phase separation suggesting that the molecules have a limited tendency to aggregate or crystallize in the blends with [60]PCBM. In accordance, the X-ray diffractograms of pure drop-cast films of these compounds show small signs of crystallinity only (Fig. S13 and S14, ESI†). In these cases thermal annealing helps to induce crystallization and phase separation. For all other molecules listed in Table 6, thermal annealing results in lower PCE. For DTT-L and BDT-L we attribute this to the fact that these compounds already give significant phase separation in as-cast films due to spinodal demixing and a larger critical crystallization nucleus as discussed in Section 2.3.2. In these cases thermal annealing enhances the phase separation further, resulting in a loss of photocurrent and PCE (cf. Tables S4 and S5†). For BDT-2C6-S we discussed in Section 2.3.3 that thermal annealing also enhances the domain size (cf. Fig. 5c and d). For the remaining two molecules listed in Table 6, DTT-S and BDT-S, the explanation is less clear. In both cases thermal annealing causes a significant reduction of PCE as a consequence of a reduction of J_{sc} and FF. The reduction of the FF is appreciable; from 0.44 to 0.36 for DTT-S (Table S2, ESI†) and from 0.53 to 0.46 for BDT-S (Table S3, ESI†). The only other molecule in this series that gives a similarly large decrease in FF upon thermal annealing is BDT-2C6-S where the FF decreases from 0.35 to 0.24 (Table S7, ESI†). In all other cases the FF remains constant or is significantly increased. Another common feature of the annealed blends of DTT-S, BDT-S and BDT-2C6-S with [60]PCBM is the appearance of longer, worm-like features in the TEM images (see Fig. S3b, S4b, and S9b, ESI†). This suggests that the morphology of these films has a common underlying structure, e.g. vertical stratification, that deteriorates the FF.

Table 5 Uncorrected PCE^a values for bis-DPP:[60]PCBM films deposited using different co-solvents

Material	No co-solvent	DIO (0.2%)	o-DCB (0.2%)	1-CN (0.2%)
TT-S	2.9^b	1.8	2.3^b	4.8^b
DTT-S	2.2	1.8	1.8	2.5
DTT-L	1.1	1.2	1.7	2.6
BDT-S	1.7	1.5	1.3^c	2.7
BDT-L	0.8^b	1.2^b	1.1^b	2.3
BDT-EH-S	4.3^b	4.5^{b,d}	3.4^c	4.3^b
BDT-2C6-S	1.5^b	2.5^e	1.1	1.2
BDT-EH-S-BT	4.6^b	3.7	4.0^b	4.3^b

^{a} These PCE values were obtained from the J–V characteristics under white light illumination and can differ from the more accurate values mentioned in Tables 2–5 where the J_{sc} was obtained from integration of the EQE spectrum. ^{b} After thermal annealing at 110 °C for 5 or 10 min. ^{c} Using 0.5% o-DCB. ^{d} Using 0.1% DIO. ^{e} Using 0.3% DIO.

Table 6 Uncorrected PCE^a values for bis-DPP:[60]PCBM films before and after annealing

Material	Solvent	As cast	Annealed^b	+/−
TT-S	CHCl$_3$/1-CN (0.2%)	3.9	4.8	+
DTT-S	CHCl$_3$/1-CN (0.2%)	2.5	1.1	−
DTT-L	CHCl$_3$/1-CN (0.2%)	2.6	1.6	−
BDT-S	CHCl$_3$/1-CN (0.2%)	2.7	1.8	−
BDT-L	CHCl$_3$/1-CN (0.2%)	2.3	1.9	−
BDT-EH-S	CHCl$_3$/1-CN (0.2%)	2.5	4.3	+
BDT-2C6-S	CHCl$_3$/DIO (0.2%)	1.9	0.5	−
BDT-EH-S-BT	CHCl$_3$	4.2	4.6	+

^{a} These PCE values were obtained from the J–V characteristics under white light illumination and can differ from the more accurate values mentioned in Tables 1–4, where the J_{sc} was obtained from integration of the EQE spectrum. ^{b} At 110 °C for 5 or 10 min.

3. Conclusions

The effects of structural variations in the core, the side chains, and the end groups on the photovoltaic performance has been studied in a series of bis-DPP small molecules for organic solar cells in an attempt to understand structure – processing – morphology – performance relationships. Molecules BDT-EH-S

10538 | J. Mater. Chem. A, 2016, **4**, 10532–10541

This journal is © The Royal Society of Chemistry 2016

and BDT-EH-S-BT reach PCEs of ∼4.3% in blends with [60] PCBM after thermal annealing. Each of these blends has a morphology that features small, but distinct domains. For TT-S the PCE also reaches 4.3% in combination with [60]PCBM. In this case TEM gives no clear evidence of phase separation, but AFM shows distinct surface features.

Molecules with longer side chains (DTT-L and BDT-L) give coarser phase separation because they can give rise to spinodal demixing of the solution and because their critical nucleus size is larger. To achieve small domain sizes that provide efficient exciton dissociation and good efficiency, the solubility of the compounds is a critical parameter that should not be too high.

For the bis-DPP molecules the use of co-solvent results in an improved solar cell performance after spin coating. While co-solvents such as DIO and o-DCB can be used, 1-CN provided in general the best performance. For the bis-DPPs molecules the amount of co-solvent required for best performance is usually 0.2 vol%, and hence much less than typical values (3 vol% to 10 vol%) needed for reaching optimized performance for DPP polymers.[107–109] For DPP polymers we have previously established that the co-solvent induces polymer aggregation in the last stages of the drying where the total solvent content has decreased to about 80% and the remaining solvent fraction is mainly comprised of the high-boiling co-solvent.[108] At the low concentrations of co-solvent used for the bis-DPP molecules, the mechanism is likely to be different, because the amount of co-solvent in the casting solution is initially of the same order, or even less, as that of the semiconductors. Thus the film will be virtually dry before the co-solvent has become the main solvent component.

Thermal annealing improves the efficiency of the cells of TT-s, BDT-EH-S and BDT-EH-S-BT where casting results in intimately mixed films. By blending with [60]PCBM the crystallization of these bis-DPP is retarded and it can be accomplished by thermal annealing. However, thermal annealing can also decrease the device performance. This occurs when the initial phase separation is already coarse (DTT-L and BDT-L), but also can also happen in cases (DTT-S, BDT-S, and BDT-2C6-S) where the initial morphology is finely mixed. In the latter cases we find that the thermal annealing results in a significantly reduced fill factor, which signifies that charge collection is hampered, despite a more crystalline morphology.

With these results, some structural factors for designing successful bis-DPP molecules for solution-processed organic solar cells emerge. Solubility and tendency to crystallize are important to achieve the small domain size (10–20 nm) which is necessary for a good performance. Yet, strong effects are seen with rather subtle structural changes and, hence, evolutionary rather than rational design of successful molecules will remain the most likely option to progress in this field for some time.

Acknowledgements

Notes and references

1 S.-H. Liao, H.-J. Jhuo, P.-N. Yeh, Y.-S. Cheng, Y.-L. Li, Y.-H. Lee, S. Sharma and S.-A. Chen, *Sci. Rep.*, 2014, **4**, 6813.

2 Y. Liu, J. Zhao, Z. Li, C. Mu, W. Ma, H. Hu, K. Jiang, H. Lin, H. Ade and H. Yan, *Nat. Commun.*, 2014, **5**, 5293.

3 J.-D. Chen, C. Cui, Y.-Q. Li, L. Zhou, Q.-D. Ou, C. Li, Y. Li and J.-X. Tang, *Adv. Mater.*, 2015, **27**, 1035–1041.

4 S. Zhang, L. Ye, W. Zhao, B. Yang, Q. Wang and J. Hou, *Sci. China: Chem.*, 2015, **58**, 248–256.

5 Z. He, B. Xiao, F. Liu, H. Wu, Y. Yang, S. Xiao, C. Wang, T. P. Russell and Y. Cao, *Nat. Photonics*, 2015, **9**, 174–179.

6 V. Vohra, K. Kawashima, T. Kakara, T. Koganezawa, I. Osaka, K. Takimiya and H. Murata, *Nat. Photonics*, 2015, **9**, 403–408.

7 K. H. Hendriks, W. Li, G. H. L. Heintges, G. W. P. van Pruissen, M. M. Wienk and R. A. J. Janssen, *J. Am. Chem. Soc.*, 2014, **136**, 11128–11133.

8 L. Lu, T. Zheng, T. Xu, D. Zhao and L. Yu, *Chem. Mater.*, 2015, **27**, 537–543.

9 H. Zong, C.-Z. Li, J. Carpenter, H. Ade and A. K.-Y. Jen, *J. Am. Chem. Soc.*, 2015, **137**, 7616–7619.

10 T. Vangerven, P. Verstappen, J. Drijkoningen, W. Dierckx, S. Himmelberger, A. Salleo, D. Vanderzande, W. Maes and J. V. Manca, *Chem. Mater.*, 2015, **27**, 3726–3732.

11 Y. Lin, Y. Li and X. Zhan, *Chem. Soc. Rev.*, 2012, **41**, 4245–4272.

12 Y. Lin and X. Zhan, *Acc. Chem. Res.*, 2016, **49**, 175–183.

13 Y. Sun, G. C. Welch, W. L. Leong, C. J. Takacs, G. C. Bazan and A. J. Heeger, *Nat. Mater.*, 2012, **11**, 44–48.

14 S. Roquet, A. Cravino, P. Leriche, O. Aleveque, P. Frere and J. Roncali, *J. Am. Chem. Soc.*, 2006, **128**, 3459–3466.

15 N. M. Kronenberg, M. Deppisch, F. Würthner, H. W. A. Lademann, K. Deing and K. Meerholz, *Chem. Commun.*, 2008, 6489–6491.

16 U. Mayerhöffer, K. Deing, K. Gruß, H. Braunschweig, K. Meerholz and F. Würthner, *Angew. Chem., Int. Ed.*, 2009, **48**, 8776–8779.

17 A. K. K. Kyaw, D. H. Wang, D. Wynands, J. Zhang, T.-Q. Nguyen, G. C. Bazan and A. J. Heeger, *Nano Lett.*, 2013, **13**, 3796–3801.

18 B. Kan, Q. Zhang, M. Li, X. Wan, W. Ni, G. Long, Y. Wang, X. Yang, H. Feng and Y. Chen, *J. Am. Chem. Soc.*, 2014, **136**, 15529–15532.

19 B. Kan, M. Li, Q. Zhang, F. Liu, X. Wan, Y. Wang, W. Ni, G. Long, X. Yang, H. Feng, Y. Zuo, M. Zhang, F. Huang, Y. Cao, T. P. Russell and Y. Chen, *J. Am. Chem. Soc.*, 2015, **137**, 3886–3893.

20 H. Bronstein, Z. Chen, R. S. Ashraf, W. Zhang, J. Du, J. R. Durrant, P. S. Tuladhar, K. Song, S. E. Watkins, Y. Geerts, M. M. Wienk, R. A. J. Janssen, T. Anthopoulos,

This journal is © The Royal Society of Chemistry 2016

J. Mater. Chem. A, 2016, **4**, 10532–10541 | **10539**

H. Sirringhaus, M. Heeney and I. McCulloch, *J. Am. Chem. Soc.*, 2011, **133**, 3272–3275.

21 K. H. Hendriks, G. H. L. Heintges, V. S. Gevaerts, M. M. Wienk and R. A. J. Janssen, *Angew. Chem., Int. Ed.*, 2013, **52**, 8341–8344.

22 K. H. Hendriks, W. Li, M. M. Wienk and R. A. J. Janssen, *J. Am. Chem. Soc.*, 2014, **136**, 12130–12136.

23 W. Li, K. H. Hendriks, M. M. Wienk and R. A. J. Janssen, *Acc. Chem. Res.*, 2016, **49**, 78–85.

24 C. B. Nielsen, M. Turbiez and I. McCulloch, *Adv. Mater.*, 2013, **25**, 1859–1880.

25 Z. Yi, S. Wang and Y. Liu, *Adv. Mater.*, 2015, **27**, 3589–3606.

26 B. Tamayo, B. Walker and T.-Q. Nguyen, *J. Phys. Chem. C*, 2008, **112**, 11545–11551.

27 B. Walker, A. B. Tamayo, X.-D. Dang, P. Zalar, J. H. Seo, A. Garcia, M. Tantiwiwat and T.-Q. Nguyen, *Adv. Funct. Mater.*, 2009, **19**, 3063–3069.

28 A. B. Tamayo, X.-D. Dang, B. Walker, J. Seo, T. Kent and T.-Q. Nguyen, *Appl. Phys. Lett.*, 2009, **94**, 103301.

29 O. P. Lee, A. T. Yiu, P. M. Beaujuge, C. H. Woo, T. W. Holcombe, J. E. Millstone, J. D. Douglas, M. S. Chen and J. M. J. Fréchet, *Adv. Mater.*, 2011, **23**, 5359–5363.

30 B.-S. Jeong, H. Choi, N. Cho, H. M. Ko, W. Lim, K. Song, J. K. Lee and J. Ko, *Sol. Energy Mater. Sol. Cells*, 2011, **95**, 1731–1740.

31 Y. Zhang, X.-D. Dang, C. Kim and T.-Q. Nguyen, *Adv. Energy Mater.*, 2011, **1**, 610–617.

32 J. Mei, K. R. Graham, R. Stadler, S. P. Tiwari, H. Cheun, J. Shim, M. Yoshi, C. Nuckolls, B. Kippelen, R. K. Castellano and J. R. Reynolds, *Chem. Mater.*, 2011, **23**, 2285–2288.

33 W. Kylberg, P. Sonar, J. Heier, J.-N. Tisserant, C. Müller, F. Nüesch, Z.-L. Chen, A. Dodabalapur, S. Yoon and R. Hany, *Energy Environ. Sci.*, 2011, **4**, 3617–3624.

34 E. Ripaud, D. Demeter, T. Rousseau, E. Boucard-Cétol, M. Allain, R. Po, P. Leriche and J. Roncali, *Dyes Pigm.*, 2012, **95**, 126–133.

35 Y. Lin, P. Cheng, Y. Li and X. Zhan, *Chem. Commun.*, 2012, **48**, 4773–4775.

36 Y. Liu, X. Du, Z. Xiao, J. Cao, S. Tan, Q. Zuo and L. Ding, *Synth. Met.*, 2012, **162**, 1665–1671.

37 J. H. Liu, B. Walker, A. Tamayo, Y. Zhang and T. Q. Nguyen, *Adv. Funct. Mater.*, 2013, **23**, 47–56.

38 H. Wang, F. Liu, L. Bu, J. Gao, C. Wang, W. Wei and T. P. Russell, *Adv. Mater.*, 2013, **25**, 6519–6525.

39 V. S. Gevaerts, E. M. Herzig, M. Kirkus, K. H. Hendriks, M. M. Wienk, J. Perlich, P. Müller-Buschbaum and R. A. J. Janssen, *Chem. Mater.*, 2014, **26**, 916–926.

40 Q.-R. Yin, J.-S. Miao, Z. Wu, Z.-F. Chang, J.-L. Wang, H.-B. Wu and Y. Cao, *J. Mater. Chem. A*, 2015, **3**, 11575–11586.

41 J.-L. Wang, Z. Wu, J.-S. Miao, K.-K. Liu, Z.-F. Chang, R.-B. Zhang, H.-B. Wu and Y. Cao, *Chem. Mater.*, 2015, **27**, 4338–4348.

42 M. E. Farahat, D. Patra, C.-H. Lee and C.-W. Chu, *ACS Appl. Mater. Interfaces*, 2015, **7**, 22542–22550.

43 S. Loser, C. J. Bruns, H. Miyauchi, R. C. Ortiz, A. Facchetti, S. I. Stupp and T. J. Marks, *J. Am. Chem. Soc.*, 2011, **21**, 8142–8145.

44 S. Loser, H. Miyauchi, J. W. Hennek, J. Smith, C. Huang, A. Facchetti and T. J. Marks, *Chem. Commun.*, 2012, **48**, 8511–8513.

45 P.-L. T. Boudreault, J. W. Hennek, S. Loser, R. P. Ortiz, B. J. Eckstein, A. Facchetti and T. J. Marks, *Chem. Mater.*, 2012, **24**, 2929–2942.

46 D. Sahu, C.-H. Tsai, H.-Y. Wei, K-C. Ho, F.-C. Chang and C.-W. Chu, *J. Mater. Chem.*, 2012, **22**, 7945–7953.

47 W. W. H. Wong, J. Subbiah, S. R. Puniredd, B. Purushothaman, W. Pisula, N. Kirby, K. Müllen, D. J. Jones and A. B. Holmes, *J. Mater. Chem.*, 2012, **22**, 21131–21137.

48 J. W. Lee, Y. S. Choi and W. H. Jo, *Org. Electron.*, 2012, **13**, 3060–3066.

49 J. K. Park, C. Kim, B. Walker, T.-Q. Nguyen and J. H. Seo, *RSC Adv.*, 2012, **2**, 2232–2234.

50 J.-Y. Pan, L.-J. Zuo, X.-L. Hu, W.-F. Fu, M.-R. Chen, L. Fu, X. Gu, H.-Q. Shi, M.-M. Shi, H.-Y. Li and H.-Z. Chen, *ACS Appl. Mater. Interfaces*, 2013, **5**, 972–980.

51 J. Huang, C. Zhan, X. Zhang, Y. Zhao, Z. Lu, H. Jia, B. Jiang, J. Ye, S. Zhang, A. Tang, Y. Liu, Q. Pei and J. Yao, *ACS Appl. Mater. Interfaces*, 2013, **5**, 2033–2039.

52 Y. Lin, Y. Li and X. Zhan, *Adv. Energy Mater.*, 2013, **3**, 724–728.

53 Y. Lin, L. Ma, Y. Li, Y. Liu, D. Zhu and X. Zhan, *Adv. Energy Mater.*, 2013, **3**, 1166–1170.

54 C. M. Proctor, C. Kim, D. Neher and T.-Q. Nguyen, *Adv. Funct. Mater.*, 2013, **23**, 3584–3594.

55 B. Walker, J. Liu, C. Kim, G. C. Welch, J. K. Park, J. Lin, P. Zalar, C. M. Proctor, J. H. Seo, G. C. Bazan and T.-Q. Nguyen, *Energy Environ. Sci.*, 2013, **6**, 952–962.

56 Y.-A. Duan, Y. Geng, H.-B. Li, J.-L. Jin, Y. Wu and Z.-M. Su, *J. Comput. Chem.*, 2013, **34**, 1611–1619.

57 L. Li, Y. Huang, J. Peng, Y. Cao and X. Peng, *J. Mater. Chem. A*, 2013, **1**, 2144–2150.

58 A. Tang, L. Li, Z. Lu, J. Huang, H. Jia, C. Zhan, Z. Tan, Y. Li and J. Yao, *J. Mater. Chem. A*, 2013, **1**, 5747–5757.

59 W. Li, M. Kelchtermans, M. M. Wienk and R. A. J. Janssen, *J. Mater. Chem. A*, 2013, **1**, 15150–15157.

60 L. Zhang, S. Zeng, L. Yin, C. Ji, K. Li, Y. Li and Y. Wang, *New J. Chem.*, 2013, **37**, 632–639.

61 Y. S. Choi and W. H. Jo, *Org. Electron.*, 2013, **14**, 1621–1628.

62 A. Guerrero, S. Loser, G. Garcia-Belmonte, C. J. Bruns, J. Smith, H. Miyauchi, S. I. Stupp, J. Bisquert and T. J. Marks, *Phys. Chem. Chem. Phys.*, 2013, **15**, 16456–16462.

63 J. Huang, X. Wang, X. Zhang, Z. Niu, Z. Lu, B. Jiang, Y. Sun, C. Zhan and J. Yao, *ACS Appl. Mater. Interfaces*, 2014, **6**, 3853–3862.

64 Q.-C. Yu, W.-F. Fu, J.-H. Wan, X.-F. Wu, M.-M. Shi and H.-Z. Chen, *ACS Appl. Mater. Interfaces*, 2014, **6**, 5798–5809.

65 S.-Y. Liu, W.-Q. Liu, J.-Q. Xu, C.-C. Fan, W.-F. Fu, J. Ling, J.-Y. Wu, M.-M. Shi, A. K.-Y. Jen and H.-Z. Chen, *ACS Appl. Mater. Interfaces*, 2014, **6**, 6765–6775.

66 M. Jung, Y. Yoon, J. H. Park, W. Cha, A. Kim, J. Kang, S. Gautam, D. Seo, J. H. Cho, H. Kim, J. Y. Choi, K. H. Chae, K. Kwak, H. J. Son, M. J. Ko, H. Kim,

10540 | *J. Mater. Chem. A*, 2016, **4**, 10532–10541

This journal is © The Royal Society of Chemistry 2016

D.-K. Lee, J. Y. Kim, D. H. Choi and B. S. Kim, *ACS Nano*, 2014, **8**, 5988–6003.

67 W. Shin, T. Yasuda, Y. Hidaka, G. Watanabe, R. Arai, K. Nasu, T. Yamaguchi, W. Murakami, K. Makita and C. Adachi, *Adv. Energy Mater.*, 2014, **4**, 1400879.

68 Z. Niu, X. Wang, J. Huang, A. Tang, Y. Sun and C. Zhan, *Asian J. Org. Chem.*, 2014, **3**, 948–952.

69 Q.-C. Yu, W.-F. Fu, H.-Y. Wang, X.-F. Wu, J.-H. Wan, M.-M. Shi and H.-Z. Chen, *Asian J. Org. Chem.*, 2014, **3**, 984–993.

70 T. Harschneck, N. Zhou, E. F. Manley, S. J. Lou, X. Yu, M. R. Butler, A. Timalsina, R. Turrisi, M. A. Ratner, L. X. Chen, R. P. H. Chang, A. Facchetti and T. J. Marks, *Chem. Commun.*, 2014, **50**, 4099–4101.

71 Z. Du, W. Chen, S. Wen, S. Qiao, Q. Liu, D. Ouyang, N. Wang, X. Bao and R. Yang, *ChemSusChem*, 2014, **7**, 3319–3327.

72 H. Qin, L. Li, F. Guo, S. Su, J. Peng, Y. Cao and X. Peng, *Energy Environ. Sci.*, 2014, **7**, 1397–1401.

73 H. Bai, P. Cheng, Y. Wang, L. Ma, Y. Li, D. Zhu and X. Zhan, *J. Mater. Chem. A*, 2014, **2**, 778–784.

74 W. Liu, S. Liu, N. K. Zawack, T. R. Andersen, P. Cheng, L. Fu, M. Chen, W. Fu, E. Bundgaard, M. Jørgensen, X. Zhan, F. C. Krebs and H. Chen, *J. Mater. Chem. A*, 2014, **2**, 19809–19814.

75 Y. Chen, A. Tang, X. Zhang, Z. Lu, J. Huang, C. Zhan and J. Yao, *J. Mater. Chem. A*, 2014, **2**, 1869–1876.

76 C. Yu, Z. Liu, Y. Yang, J. Yao, Z. Cai, H. i. Luo, G. Zhang and D. Zhang, *J. Mater. Chem. C*, 2014, **2**, 10101–10109.

77 S. Y. Liu, W. F. Fu, J. Q. Xu, C. C. Fan, H. Jiang, M. Shi, H. Y. Li, J. W. Chen, Y. Cao and H. Z. Chen, *Nanotechnology*, 2014, **25**, 014006.

78 Y. Zhang, H. Tan, M. Xiao, X. Bao, Q. Tao, Y. Wang, Y. Liu, R. Yang and W. Zhu, *Org. Electron.*, 2014, **15**, 1173–1183.

79 H.-F. Feng, W.-F. Fu, L. Li, Q.-C. Yu, H. Lu, J.-H. Wan, M.-M. Shi, H. Z. Chen, Z. Tan and Y. Li, *Org. Electron.*, 2014, **15**, 2575–2586.

80 A. M. Raynor, A. Gupta, H. Patil, A. Bilic and S. V. Bhosale, *RSC Adv.*, 2014, **4**, 57635–57638.

81 H. Patil, A. Gupta, A. Bilic, S. V. Bhosale and S. V. Bhosale, *Tetrahedron Lett.*, 2014, **55**, 4430–4432.

82 X. Duan, M. Xiao, J. Chen, X. Wang, W. Peng, L. Duan, H. Tan, G. Lei, R. Yang and W. Zhu, *ACS Appl. Mater. Interfaces*, 2015, **7**, 18292–18299.

83 J.-H. Kim, J. B. Park, H. Yang, I. H. Jung, S. C. Yoon, D. Kim and D.-H. Hwang, *ACS Appl. Mater. Interfaces*, 2015, **7**, 23866–23875.

84 A. Tang, C. Zhan and J. Yao, *Adv. Energy Mater.*, 2015, **5**, 1500059.

85 X.-F. Wu, W.-F. Fu, Z. Xu, M. Shi, F. Liu, H.-Z. Chen, J.-H. Wan and T. P. Russell, *Adv. Funct. Mater.*, 2015, **25**, 5954–5966.

86 Z. Tang, B. Liu, A. Melianas, J. Bergqvist, W. Tress, Q. Bao, D. Qian, O. Inganäs and F. Zhang, *Adv. Mater.*, 2015, **27**, 1900–1907.

87 J. W. Jung, T. P. Russell and W. H. Jo, *Chem. Mater.*, 2015, **27**, 4865–4870.

88 J. W. Jung and W. H. Jo, *Chem. Mater.*, 2015, **27**, 6038–6043.

89 M. Jung, D. Seo, K. Kwak, A. Kim, W. Cha, H. Kim, Y. Yoon, M. J. Ko, D.-K. Lee, J. Y. Kim, H. J. Son and B. S. Kim, *Dyes Pigm.*, 2015, **115**, 23–34.

90 K. Gao, L. Li, T. Lai, L. Xiao, Y. Huang, F. Huang, J. Peng, Y. Cao, F. Liu, T. Russell, R. Janssen and X. Peng, *J. Am. Chem. Soc.*, 2015, **137**, 7282–7285.

91 B. Chen, Y. Yang, P. Cheng, X. Chen, X. Zhan and J. Qin, *J. Mater. Chem. A*, 2015, **3**, 6894–6900.

92 D. Qian, B. Liu, S. Wang, S. Himmelberger, M. Linares, M. Vagin, C. Müller, Z. Ma, S. Fabiano, M. Berggren, A. Salleo, O. Inganäs, Y. Zou and F. Zhang, *J. Mater. Chem. A*, 2015, **3**, 24349–24357.

93 N. Zhou, S. Vegiraju, X. Yu, E. F. Manley, M. R. Butler, M. J. Leonardi, P. Guo, W. Zhao, Y. Hu, K. Prabakaran, R. P. H. Chang, M. A. Ratner, L. X. Chen, A. Facchetti, M. C. Chen and T. J. Marks, *J. Mater. Chem. C*, 2015, **3**, 8932–8941.

94 Y. Zhang, M. Xiao, N. Su, J. Zhong, H. Tan, Y. Wang, Y. Liu, Y. Pei, R. Yang and W. Zhu, *Org. Electron.*, 2015, **17**, 198–207.

95 W. Liu, H. Shi, W. Fu, L. Zuo, L. Wang and H. Chen, *Org. Electron.*, 2015, **25**, 219–224.

96 S. Wang, J. Yang, Z. Zhang, Y. Hu, X. Cao, H. Li, Y. Tao, Y. Li and W. Huang, *RSC Adv.*, 2015, **5**, 68192–68199.

97 T. W. Lee, D. H. Lee, T. R. Hong, J. Shin, M. J. Cho and D. H. Choi, *Synth. Met.*, 2015, **206**, 24–32.

98 J. Chen, M. Xiao, F. Meng, L. Duan, H. Tan, Y. Wang, Y. Liu, R. Yang and W. Zhu, *Synth. Met.*, 2015, **199**, 400–407.

99 D. Yu, Y. Liu, M. Xiao, Q. Fan, W. Su, X. Li, H. Tan, Y. Wang, R. Yang and W. Zhu, *Dyes Pigm.*, 2016, **125**, 151–158.

100 X. Liu, C. Huang, W. Shen, R. He and M. Li, *J. Mol. Model.*, 2016, **22**, 15.

101 T. Liang, L. Xiao, C. Liu, K. Gao, H. Qin, Y. Cao and X. Peng, *Org. Electron.*, 2016, **29**, 127–134.

102 J. Chen, M. Xiao, L. Duan, Q. Wang, H. Tan, N. Su, Y. Liu, R. Yang and W. Zhu, *Phys. Chem. Chem. Phys.*, 2016, **18**, 1507–1515.

103 Y. Lin, J. Wang, T. Li, Y. Wu, C. Wang, L. Han, Y. Yao, W. Ma and X. Zhan, *J. Mater. Chem. A*, 2016, **4**, 1486–1494.

104 J. Wang, K. Shi, Y. Suo, Y. Lin, G. Yu and X. Zhan, *J. Mater. Chem. C*, 2016, **4**, 3781–3791.

105 C. Lu and W. C. Chen, *Chem.–Asian J.*, 2013, **8**, 2813–2821.

106 P. W. M. Blom, V. D. Mihailetchi, L. J. A. Koster and D. E. Markov, *Adv. Mater.*, 2007, **19**, 1551–1566.

107 S. Kouijzer, J. J. Michels, M. van den Berg, V. S. Gevaerts, M. Turbiez, M. M. Wienk and R. A. J. Janssen, *J. Am. Chem. Soc.*, 2013, **135**, 12057–12067.

108 J. J. van Franeker, M. Turbiez, W. Li, M. M. Wienk and R. A. J. Janssen, *Nat. Commun.*, 2015, **6**, 6229.

109 J. J. van Franeker, G. H. L. Heintges, C. Schaefer, G. Portale, W. Li, M. M. Wienk, P. van der Schoot and R. A. J. Janssen, *J. Am. Chem. Soc.*, 2015, **137**, 11783–117945.

110 C. J. Takacs, Y. Sun, G. C. Welch, L. A. Perez, X. Liu, W. Wen, G. C. Bazan and A. J. Heeger, *J. Am. Chem. Soc.*, 2012, **134**, 16597–16606.

111 H. Wang, F. Liu, L. Bu, J. Gao, C. Wang, W. Wei and T. P. Russell, *Adv. Mater.*, 2013, **25**, 6519–6525.

This journal is © The Royal Society of Chemistry 2016

J. Mater. Chem. A, 2016, **4**, 10532–10541 | 10541